International Journal of Nanoelectronics and Materials
IJNeaM
ISSN 1985-5761 | E-ISSN 2232-1535

Impact of Nb Content on Oxide Growth Characteristics of HR120 Alloy in the Fe-40Ni-24Cr System Under Isothermal Oxidation Conditions

Noraziana Parimin[a,*], Esah Hamzah[b], Astuty Amrin[c], and Kurnia Hastuti[d]

[a]*Materials Department, Faculty of Chemical Engineering & Technology, Universiti Malaysia Perlis (UniMAP), 02600 Arau, Perlis, Malaysia*
[b]*Faculty of Mechanical Engineering, Universiti Teknologi Malaysia (UTM), 81310 Skudai, Johor, Malaysia*
[c]*Razak Faculty of Technology and Informatics, UTM Kuala Lumpur, 54100 Kuala Lumpur, Malaysia*
[d]*Mechanical Engineering Department, Faculty of Engineering, Universitas Islam Riau, Jl. Kaharuddin Nasution No 113 Pekanbaru, Indonesia*
**Corresponding author. E-mail: noraziana@unimap.edu.my*

Received 31 Jul 2025, Revised 3 Nov 2025, Accepted 21 May 2025

ABSTRACT

The impact of Nb content on the characteristics of oxide scale formation was studied during isothermal oxidation tests of the HR120 Fe-40Ni-24Cr alloy. The oxidation kinetics, phase analysis, and surface morphology were studied using samples with low grain diameter (LGD) and high grain diameter (HGD) obtained by heat treatment at 1050 °C and 1150 °C, respectively. The LGD and HGD samples were then subjected to isothermal oxidation tests at 500 °C for 500 hours. The oxidation kinetics were measured by tracking the time for weight changeovers. Phase analysis was performed using X-ray diffraction (XRD), and surface morphology was examined using scanning electron microscopy (SEM) and field-emission SEM (FESEM) with energy-dispersive X-ray (EDX) analysis. The oxidation kinetic plots exhibited an increasing weight gain trend for LGD and HGD samples, and followed a parabolic rate law. A lower parabolic rate constant was recorded by LGD sample of 7.38×10^{-9} $mg^2 \cdot cm^{-4} \cdot s^{-1}$, indicating a lower oxidation rate, hence having good oxidation resistance. Phase analysis recorded Cr_2O_3 and $MnCr_2O_4$ oxides formed on both samples. Surface morphology analysis revealed a uniform oxide layer coexisting with a protruding Nb-rich oxide structure, further confirmed by EDX, and the LGD sample exhibited good scale integrity. The HGD samples displayed overgrown protruding oxide structures with non-adherent oxide scale, with evidence of oxide exfoliation. These findings support the proposed oxide diffusion mechanism, indicating that Nb content has the greatest impact on oxide growth in the HGD samples.

Keywords: *HR120 alloy, Fe-40Ni-24Cr Ni-based alloy, Isothermal oxidation*

1. INTRODUCTION

Ni-based Fe-Ni-Cr alloys, such as HR120, are widely employed in high-temperature industrial environments, including gas turbine engines, power generation systems, petrochemical processing units, and thermal treatment equipment, where components are routinely exposed to oxidizing, carburising, and sulfidizing atmospheres [1-2]. HR120 alloy has been used in furnace components, heat exchanger sections, radiant tubes and reformer tubes due to its thermal stability, creep strength and resistance to scale formation during prolonged service at temperatures above 1000 °C. The Fe-40Ni-24Cr alloy system, from which the primary composition of HR120 was developed, offers a balanced combination of excellent oxidation and carburization resistance and excellent mechanical properties, making it suitable for use in industrial heating and heat treatment operations such as annealing, sintering and solution treatment processes [3-4]. Under the operating conditions described above, it is necessary to use alloys that resist oxidation and maintain structural integrity by preventing degradation phenomena, such as oxide exfoliation or internal oxidation, which can affect component life and reliability in long-term service. For these applications, oxidation resistance is one of the most critical properties governing long-term performance and durability [5-6].

The Fe-40Ni-24Cr alloy mainly comprises Fe, Ni and Cr. Cr would act as the principal oxide former, which forms a continuous chromia Cr_2O_3 layer during high-temperature oxidation, exhibiting slow growth rate and providing effective barrier against oxidation in harsh atmospheres, and serving as the main protection barrier by limiting oxygen diffusion into the substrate [7-8]. At high temperatures, the performance and resilience of the Fe-40Ni024Cr system are sturdily governed by the formation and stability of protective oxide scales. Previous studies have also reported the development of spinel oxides in chromia-forming alloys, which act cooperatively with Cr_2O_3 to further enhance oxidation resistance [2,9]. The chromia layer is further strengthen by the formation of spinel oxides such as $MnCr_2O_4$, $FeCr_2O_4$, and $NiCr_2O_4$, which improve adherence and slow down further oxidation. The protective properties of these scales are crucial for ensuring long-term service life in hostile industrial atmospheres, such as heat-treatment furnaces and combustion components [10-11].

To further improve high-temperature performance, the development of stable precipitates is required to enhance oxidation and mechanical properties by adding alloying elements that act as carbide formers to the alloy system, such as Nb, Mn, and Ti [12-13]. The addition of minor amounts of Nb and Ti in the HR120 alloy contributes to strengthening through the precipitation of MC-type (metal

carbide) carbides and improves microstructural stability during service. In this context, M denotes a metal element such as Nb or Ti, and C denotes carbon. Typical MC-type precipitates of NbC, TiC and (Nb, Ti) C carbides are frequently found in Ni-based alloys and are also used as carbide reinforcements in certain metal matrix systems [14]. MC-type carbides strengthen alloys by impeding dislocations to some extent and have a beneficial effect on strengthening grain boundary phases in Ni-based alloys [15]. Nevertheless, in some circumstances, the formation of coarse Nb-rich oxide precipitates occurs during high-temperature oxidation of Nb-containing alloys, which induces localized stresses that encourage the formation of cracks, thus affecting the quality of the protective oxide scale [4]. Therefore, it is important to understand how Nb content influences the oxide growth behaviour of the HR120 alloy to optimize its performance under prolonged isothermal oxidation conditions.

Some studies have stated that Nb's strong affinity for oxygen controls its segregation and oxidation behaviour, which in turn influences the alloy's performance at high temperatures. At times, Nb contributes to the stabilization of protective oxide scales, while in others it encourages the development of localized oxide protrusions or crack initiation within the scale [14-16]. Studies on the oxidation of Ni-based superalloys have carefully documented the buildup of Cr and Nb on the alloy surface, along with the establishment of Nb-rich oxide structures [4,17]. Other findings specify the construction of a layered oxide scale characterized by a Cr-rich outer layer and a Nb-rich sublayer, as well as the enrichment of Nb in the Cr_2O_3 scale. Even though Nb has a relatively low concentration in bulk, it easily separates to the surface and oxidized under severe environments, indicating its tendency to move toward chemically active sites and participate in confined oxidation processes.

One of the recognized phenomena in high-temperature exposure of metal alloys is the formation of internal oxidation, which is prone to form underneath the external scale by inward diffusion and reacting with the substrate between the oxide-metal phase. Al and Si are the alloying elements that are predominantly prone to form internal oxide scale beneath the outermost oxide layer [18-20]. Al-rich oxide is often detected near the surface region, whereas Si-rich oxide may also form. Al-rich and Si-rich oxides contribute significantly to the overall protective effect of the scale under high-temperature condition.

The oxidation resistance of HR120 Ni-based alloys is governed by their chemical composition and strongly influenced by their microstructural characteristics, particularly grain diameter [4,21]. During high-temperature oxidation, grain diameter plays a crucial role in oxidation behaviour by controlling diffusion pathways for both metallic and oxygen species. The heat treatment process is one of the effective methods for modifying grain diameter, where the annealing temperature and duration determine the extent of recrystallization and subsequent grain coarsening [21].

Several studies have investigated the oxidation behaviour on Ni-based alloys containing Nb, focusing on effect of Nb content on the bulk alloy or on the stability of the oxide scale. Some interest has been devoted to studies focusing on the effect of Nb content on the oxide scale in relation to grain diameter. At times, the role of Nb-rich oxide protrusions and their interaction with protective chromia and their dependence on microstructural scale have not been systematically explored. The present study addresses this gap by investigating how Nb content in HR120 alloy influences oxidation kinetic, oxide phase establishment and oxide scale morphology under isothermal conditions, while explicitly comparing low-grained and high-grained diameter conditions. By relating the Nb segregation behaviour to the grain diameter-dependent diffusion pathway, thus work reveals new mechanistic insights into the development of protrusion Nb-rich oxides and their impact on the integrity of the protective scale. Moreover, a diffusion-based oxidation model is proposed to describe the sequential progression from planar to perpendicular to protruding oxide growth, providing a framework for optimizing alloy design for long-term high-temperature performance.

This study investigates the impact of Nb content on the oxidation kinetics, oxide phase formation, and oxide scale morphology of HR120 alloy in the Fe-40Ni-24Cr system under high-temperature isothermal oxidation conditions. The impact of grain diameter variation has been the primary focus of this study, which is a comparison between low and high grain diameter alloy structures. This study is about the establishment and formation of stable Nb-rich oxide structures, and then verifying its role as a protective oxide scale formation or contributing to the oxide exfoliation phenomenon. The present work provides the correlation between grain diameter, Nb segregation, and the evolution of protruding Nb-rich oxides in HR120 alloy during prolonged oxidation. Furthermore, a diffusion-based oxidation model is proposed to describe the sequential progression of planar, perpendicular, and protruding oxide growth, thereby linking microstructural evolution to oxidation kinetics.

2. METHODOLOGY

2.1. Materials

The material employed in this research is the HR120 alloy, a Ni-based alloy. The chemical composition of the alloy was determined by means of an optical emission spectrometer (OES) and is reported in weight percent (wt. %): 33.580 Fe, 40.080 Ni, 24.050 Cr, 0.718 Mn, 0.444 Nb, 0.438 Si, 0.085 Al, 0.048 C, 0.165 Co, 0.029 Ti, 0.249 Mo, and 0.114 Cu. Based on its major elemental constituents, this alloy is categorized under the Fe-40Ni-24Cr alloy system. Rectangular specimens have a final dimensions of 10 mm × 10 mm × 3 mm.

2.2. Heat Treatment Procedure

The Fe-40Ni-24Cr alloy was subjected to various heat-treatment procedures to vary the average grain diameter. Heat treatments were conducted at 1050 °C and 1150 °C for a 3-hour soag period, followed by rapid quenching in water. The average grain diameters were determined using the line intercept method in accordance with ASTM E112, yielding values of 30.25 μm and 40.17 μm for the samples treated at 1050 °C and 1150 °C, respectively. The samples are denoted as low grain diameter (LGD) and high grain diameter (HGD), corresponding to the 1050 °C and 1150 °C treatments, respectively.

2.3. Isothermal Oxidation Test

An isothermal oxidation test was carried out on the heat-treated LGD and HGD samples at 500 °C for a total period of 500 hours in laboratory air. Preceding to the test, the samples were ground using SiC sandpaper to a surface finish of P600 grit. The surface area and initial weight of each sample were determined using analytical balance. The ground samples were then exposed to isothermal oxidation at 500 °C for various time intervals, which are 100, 200, 300, 400, and 500 hours, to determine the weight change. Following each testing interval, the samples were weighed again. Oxidation kinetics were evaluated by calculating the change in weight per unit surface area as a function of oxidation time. Oxide phase identification was conducted using X-ray diffraction (XRD) on a SIEMENS diffractometer equipped with BRUKER D5000 software. Phase determination was performed using DiffracPlus Evaluation Software in conjunction with PDF-2 search/match programs. The XRD utilized a monochromatic Cu Kα radiation source (λ = 1.5406 Å), with scans implemented over a 2θ range of 22°–82. Oxide surface morphology was examined by means of a scanning electron microscope (SEM) fortified with an energy-dispersive X-ray (EDX) spectrometer model JEOL JSM-6460 LA, for samples exposed at 300 and 500 hours. Field emission scanning electron microscopy (FESEM) analysis was accomplished on samples exposed for 500 hours to provide higher-resolution surface imaging, model CARL ZEISS 35 VP. The energy range used was between 20 keV and 30 keV.

3. RESULTS AND DISCUSSION

3.1. Oxidation Kinetics

The oxidation kinetics plot revealed in Figure 1 presents the weight change per surface area as a function of time for the LGD and HGD samples over a 500-hour exposure period. Both samples exhibit an initial rapid weight gain throughout the early stage of oxidation, particularly within the first 100 hours. The curve indicates straight increase of weight pattern which is the characteristic of linear oxidation behavior which is shows by constant rate. At this period, the mechanism of oxidation comprises the nucleation process of oxide particles followed by lateral and vertical growth to develop an incessant oxide layer that protect and encapsulates the external alloy surface.

The smaller grain diameter of the LGD sample contributed to a higher grain boundary area, which allowed for rapid diffusion of oxygen and metal ions. This condition accelerated the initial development of the oxide layer, which led to the formation of a continuous and protective scale earlier in the LGD sample than in the HGD sample. This phenomenon continued until a constant and thin oxide layer completely covered the outer alloy surface. When a stable oxide layer is established, the oxidation rate slow down, and oxidation continues only by slightly increasing the scale's thickness until its achieved its most protective state. The reduction in oxidation rate is reflected by the lower overall weight gain experienced in the LGD samples as the exposure period is prolonged, reaching 0.1233 $mg{\cdot}cm^{-2}$ at 500 hours. The aforementioned condition is in line with our previous study [7], which documented rapid initial oxide scale formation in fined-grained samples, similar to the behaviour of the LGD sample in this study.

When oxidation was prolonged for 100 hours, the LGD sample exhibited a visible change from a linear curve to a parabolic curve. This phenomenon indicated that the oxide layer had increased its barrier to oxygen access. At the final stages (300-500 hours), more stable oxidation profile and significant lower weight change has been recorded by LGD sample, indicating the formation of an adherent, dense and protective oxide scale. Throughout the subsequent oxidation period, LGD sample steadily showed lower weight gain compared to HGD samples.

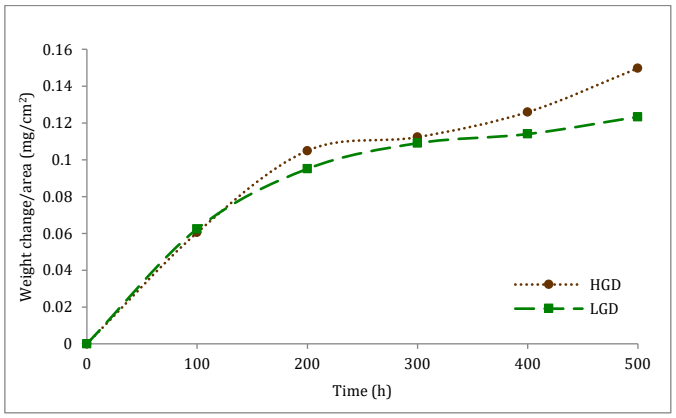

Figure 1. Weight change per unit surface area versus exposure time for low grain diameter (LGD) and high grain diameter (HGD) samples during isothermal oxidation at 500 °C for 500 hours.

On the other hand, the HGD sample has a larger grain diameter and smaller grain boundary area than the LGD sample, indicating a slower initial oxidation reaction, as recorded by the lower weight gain during the start of oxidation test up to 100 hours. The development of a continuous and protective oxide layer is delayed due to the limited number of grain boundaries in the HGD samples which reduces the diffusion paths for oxygen and metal ions, which most likely form only after the 100 hours oxidation test. Subsequently, the oxidation process continued which further increased the oxide scale in an attempt to develop an effective barrier, resulting in a higher overall weight gain occurring after 100 hours of exposure, reaching a value at 500 hours of 0.1497 mg·cm^{-2}. The HGD sample showed continuous weight gain throughout the oxidation test, indicating that oxidation continued, most likely due to the development of a porous, non-uniform oxide layer, or perhaps due to some of the oxide layers peeling off. Similar weight-gain trends have been reported by other scholars studying alloys with varying grain sizes [6], as well as in our previous study [4].

Figure 2 shows the determination of oxidation rate law behaviour for LGD and HGD samples, using oxidation kinetic plots which were further analysed. The logarithmic plot in Equation (1) was used to determine the oxidation rate law, with x denoting the change in weight per surface area, t denoting time, and m and c denoting constants. The value of m in Equation (1) determines the oxidation rate law obeyed by the sample, with m = 1 indicating a linear rate law and m = 2 indicating a parabolic rate law.

$$\log x = \frac{1}{m}\log t + c \quad (1)$$

The value of m that has been determined through the analysis of the data plotted in Figure 2, recorded a value of 2.41 for the LGD sample and 1.90 for the HGD sample. These values are in the range of 1.5 to 2.5, indicating that both LGD and HGD samples obey the parabolic rate law. Nevertheless, the value of m for the HGD sample falls below 2, indicating the possibility of oxidation, and it shows linear behaviour compared to the LGD sample. In addition, the R^2 value of the coefficient of determination for the straight trendline for both samples is 0.953 for LGD and 0.951 for HGD, indicating a strong correlation and a good fit of the recorded experimental data to the logarithmic plot. Overall, the determination of the oxidation rate law yielded consistent findings for both samples, indicating that there was a transition in the oxidation mechanism from linear behaviour at the early stage to parabolic behaviour with diffusion-controlled phenomena at the later stage, with a more ideal parabolic oxidation rate law behaviour being exhibited by the LGD sample.

After confirming that both LGD and HGD samples obeyed the parabolic rate law, the analysis is extended to the determination of the parabolic rate constant, K_p, based on Equation (2), with x denoting the change in weight per surface area, K_p denoting the parabolic rate constant, t denoting time and c denoting a constant.

$$x^2 = K_P t + c \quad (2)$$

The parabolic rate constant in Figure 3 was higher for the HGD sample, at 1.18×10^{-8} mg^2·cm^{-4}·s^{-1}, indicating a higher oxidation rate. This finding is in line with the oxidation kinetics curve of the HGD sample in Figure 1 which shows a higher weigh gain during the prolonged oxidation test. In contrast, the LGD sample showed a lower parabolic rate constant of 7.38×10^{-9} mg^2·cm^{-4}·s^{-1}, indicating a slower oxidation rate. This lower rate constant confirms that the LGD sample has superior oxidation resistance compared to the HGD sample.

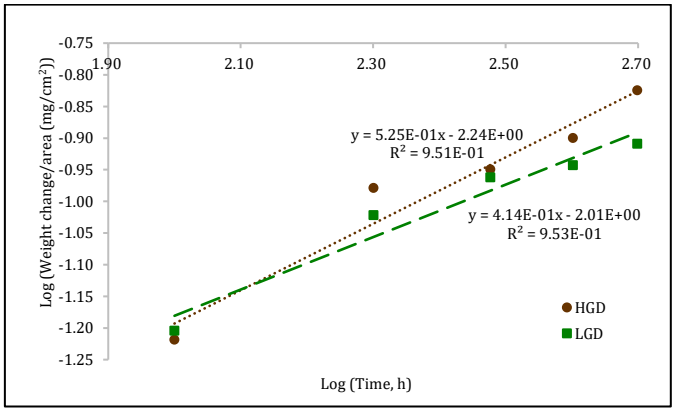

Figure 2. Log of weight change per unit surface area versus log of exposure time for low grain diameter (LGD) and high grain diameter (HGD) samples during isothermal oxidation at 500 °C for 500 hours for the determination of oxidation rate law.

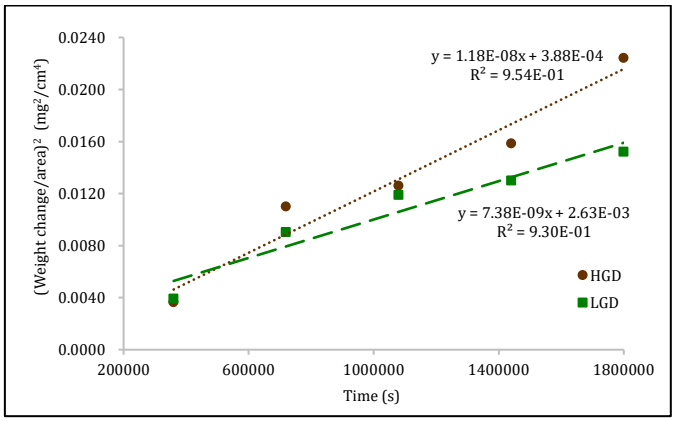

Figure 3. Square plots of the change in weight per unit surface area as a function of exposure time to determine the parabolic rate constant (K_p) for low grain diameter (LGD) and high grain diameter (HGD) samples after exposure at 500 °C for 500 hours.

3.2. Phase Analysis

Figure 4 shows the XRD patterns of the LGD and HGD samples after 300 hours of exposure. The analysis showed that the most intense diffraction peak corresponds to the base metal of the Fe-Ni-Cr alloy. In addition, other peaks of lower intensity are detected from the Cr_2O_3 and $MnCr_2O_4$ oxide phases. This indicates that a relatively thin oxide layer developed on the alloy surface, permitting deeper X-ray penetration into the underlying metal. On the other hand, Figure 5 shows the XRD patterns of the LGD and HGD samples after 500 hours of exposure. The phase identified after 500 hours of exposure was similar to that observed after 300 hours. Nevertheless, the base metal peaks after 500 hours of exposure showed a lower intensity that was significantly reduced from that after 300 hours of exposure, indicating thickening of the oxide scale. These peaks were detected as Cr_2O_3 and $MnCr_2O_4$ oxide phases.

The relative intensities of the Cr_2O_3, $MnCr_2O_4$ oxide phases and Fe-Ni-Cr base metal peaks were compared by means of semi-qualitative peak matching approach for both LGD and HGD samples at exposure period of 300 hours and 500 hours. LGD and HGD samples retains an intense base metal peaks at an oxidation time of 300 hours, which is in line with the development of a thin outer oxide layer. The HGD sample recorded sharp intense peaks of Cr_2O_3 and $MnCr_2O_4$ oxide phases at an oxidation time of 500 hours, with a significant reduction of the Fe-Ni-Cr base metal peaks. This observation indicates that a thicker oxide scale has been developed on the outer oxide layer with larger fraction of oxide. Image-based peak extraction of the 500 hours XRD traces shows that the Cr_2O_3 signal in HGD is ≈2.5-2.6× that of LGD (≈150-160% higher), consistent with its greater weight gain (0.1497 mg·cm^{-2} for HGD vs. 0.1233 mg·cm^{-2} for LGD). While these image-derived values are approximate, and full quantitative phase fractions (wt.%) would require Rietveld refinement, the combined trend from XRD and oxidation kinetics clearly indicates that HGD promotes faster oxide growth and more complete surface coverage compared to LGD.

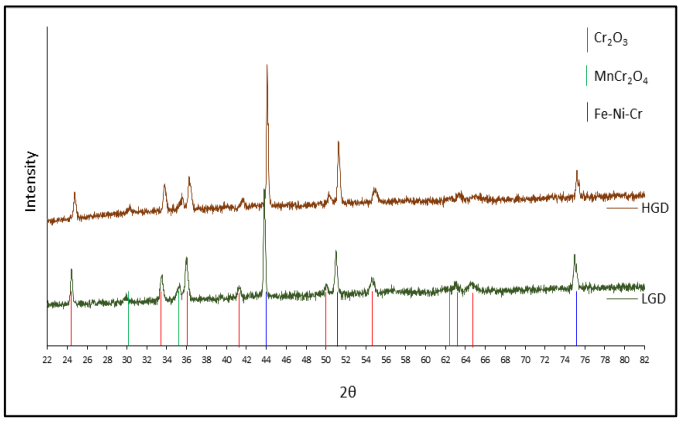

Figure 4. Comparison of X-ray diffraction (XRD) pattern for low grain diameter (LGD) and high grain diameter (HGD) samples after 300 hours of oxidation at 500 °C, arranged in stacking sequence, revealing the oxide phases formed during isothermal oxidation conditions.

The development of spinel-type oxides has been observed in our prior studies, consisting of the $MnCr_2O_4$ oxide phase which exist together with other Cr-containing spinels such as the $FeCr_2O_4$ and $NiCr_2O_4$ oxide phases. But, the diffraction peaks of these three spinal oxide phases overlap due to the similarity in their spinel crystal structures. Based on elemental EDX analysis (presented in the following results), enrichment of Mn and Cr was dominant, therefore, only $MnCr_2O_4$ peaks were labeled in the XRD results. The addition of Mn to the alloy enhances the protective properties of the $MnCr_2O_4$ oxide. This improvement occurs because Cr_2O_3 tends to volatilize during prolonged high-temperature exposure, which can lead to oxide exfoliation or the formation of a porous scale. In contrast, the presence of $MnCr_2O_4$ suppresses this effect, promoting the growth of a dense and compact oxide layer with superior protective characteristics [4]. Other studies have reported that, under certain oxidation conditions, the Ni-rich phase trapped within the $FeCr_2O_4$ spinel may either remain metallic or further oxidize, forming a more complex $(Ni,Fe,Cr)_3O_4$ spinel structure. In addition, several investigations have documented the creation of a Cr-rich oxide layer at the oxide-metal interface, typically consisting of Cr_2O_3 or mixed chromia-based phases [10].

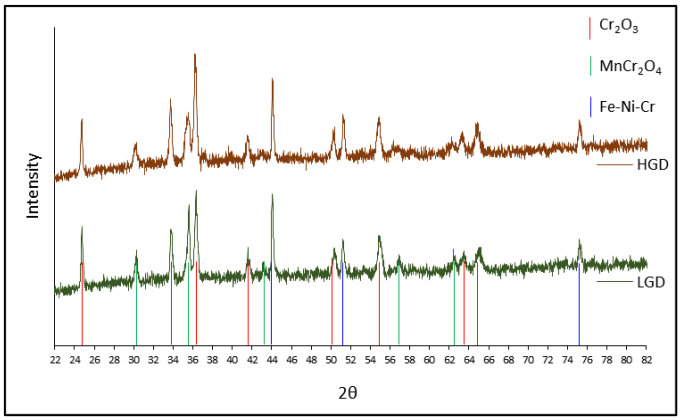

Figure 5. Comparison of X-ray diffraction (XRD) pattern for low grain diameter (LGD) and high grain diameter (HGD) samples after 500 hours of oxidation at 500 °C, arranged in stacking sequence, revealing the oxide phases formed during isothermal oxidation conditions.

3.3. Surface Morphology

Figure 6 shows SEM images of LGD and HGD samples after 300 hours of oxidation test. A uniform oxide layer with visible serrations and distributed isolated white particulate are observed on both sample surfaces. The white particle structures were evenly dispersed around the sample surface. These white particles were further inspected after an oxidation time of 500 hours. In addition, serration features are initiates from the primary grinding marks during sample preparation, indicating that a thin oxide scale had established on the outer layer.

Figure 7 shows the SEM images along with the respective EDX analyses of LGD and HGD samples after 500 hours of exposure. The SEM image of the LGD sample (Figure 7a) reveals a homogeneous oxide layer with noticeable protruding white oxide particles. EDX analysis of this white oxide particles at spot 006 (Figure 7c) detected major elements O, Cr and Nb. The Cr signal is attributed to Cr_2O_3, while Nb is most likely derived from Nb-rich oxides, which subsequent FESEM analysis (presented later) confirms a higher Nb signal intensity. Minor elements Fe and Ni were also detected, corresponding to spinel oxides $FeCr_2O_4$ and $NiCr_2O_4$, and potentially from the underlying base alloy due to the tinny oxide layer. Moreover, other elements were also detected in minor content consisting of Mn and Si. Meanwhile, analysis of the alloy matrix at spot 007 (Figure

7d) using EDX analysis recorded significant higher content of Cr and Mn elements suggesting the presence of Cr_2O_3 and $MnCr_2O_4$ oxide phases which was supported by XRD analysis results. Also, other minor contents of Fe, Ni, Si and Nb elements were recorded.

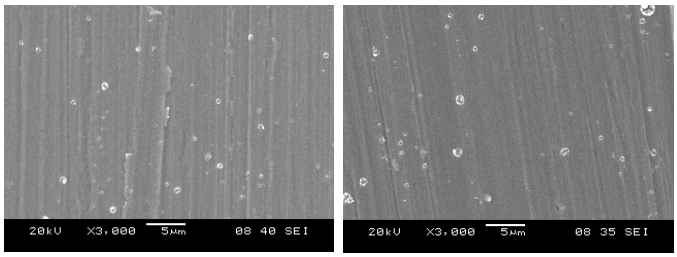

(a) (b)

Figure 6. Scanning electron microscopy (SEM) images of the surface morphology of (a) low grain diameter (LGD) and (b) high grain diameter (HGD) samples after 300 h exposure at 500 °C under isothermal oxidation.

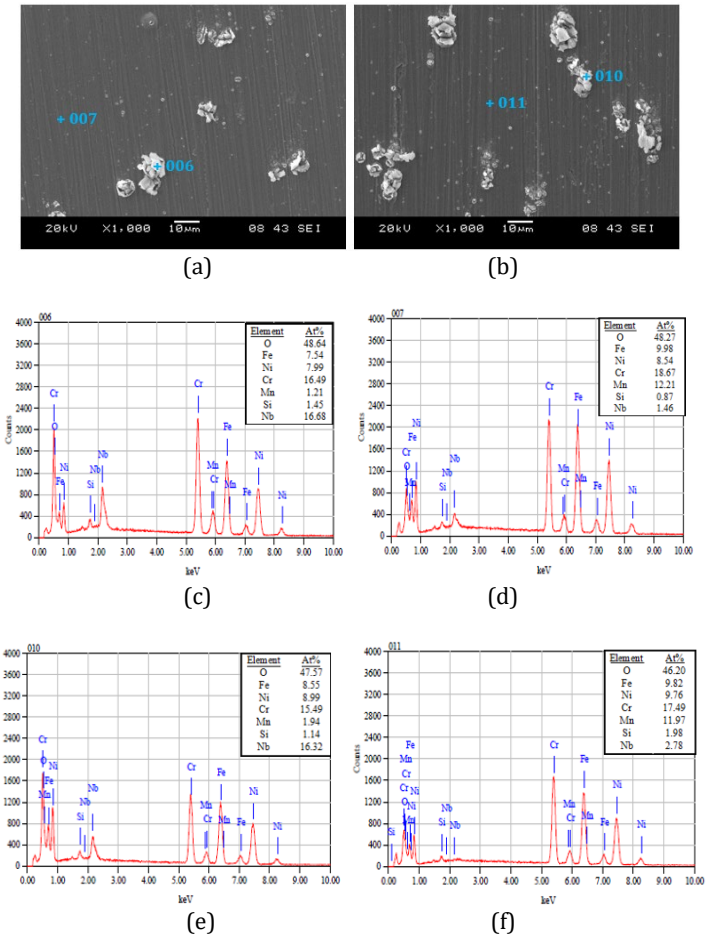

(a) (b)

(c) (d)

(e) (f)

Figure 7. Surface morphology of (a) low grain diameter (LGD) and (b) high grain diameter (HGD) samples after 500 hours of isothermal oxidation at 500 °C observed by scanning electron microscopy (SEM). The corresponding EDX spectra for the LGD sample at (c) spot 006 and (d) spot 007, and for the HGD sample at (e) spot 010 and (f) spot 011, identify the elemental composition at the indicated analysis spots.

The HGD sample was analyzed using SEM-EDX technique, resulting in several observations consisting of SEM image (Figure 7b), EDX spectra at spot 010 (Figure 7e) and spot 011 (Figure 7f). A uniform oxide layer was observed on the HGD sample with some white oxide particles scattered on the surface. The white oxide particles have a protruding structure that projecting outward from the surface. These white oxide particles were further analyzed using EDX at spot 010 resulting that were almost similar to the LGD sample which mainly composed of Cr_2O_3 and Nb-rich oxides. Also, the similar EDX results of the HGD and LGD samples in the oxide matrix region indicated that this region was established by Cr_2O_3 and $MnCr_2O_4$ oxide phases.

Surface morphology of LGD sample after 500 hours of isothermal oxidation that had been observed by FESEM technique is shown in Figure 8. The low magnification image at 500x (Figure 8a) displays the wavy surface features results from the grinding marks forms during the sample preparation process, exhibiting a moderately uniform oxide layer with scales that are not very thick. The higher magnification image at 10,000x (Figure 8b) showing

protruding white oxide particles for further analysis with EDX to verify their elemental composition.

Elemental composition analysis using EDX on the oxide matrix (Spectrum 1, Figure 8c) recorded greater contents of O, Fe, Ni and Cr elements, with lower contents of Mn and Nb elements. This finding confirms that the surface oxide consists of the existence of several oxide phases, namely Cr_2O_3, $MnCr_2O_4$, $FeCr_2O_4$, $NiCr_2O_4$, and Nb-rich oxides. Elemental composition analysis on the protruding white oxide particles (Spectrum 2, Figure 8d) based on higher magnification image (Figure 8b) recorded higher contents of O, Cr and Nb elements, indicating the establishment of Cr-rich and Nb-rich oxides in these protrusions region.

For direct comparison with the post-oxidation EDX results (reported in atomic percent), the as-received alloy composition (originally measured in wt.%) was converted to atomic percent (at. %) which are 33.50 Fe, 38.04 Ni, 25.77 Cr, 0.73 Mn, 0.27 Nb, 0.87 Si, 0.18 Al, 0.22 C, 0.16 Co, 0.03 Ti, 0.14 Mo, and 0.10 Cu. This baseline at. % composition was used to evaluate potential elemental enrichment or depletion after oxidation, particularly the Nb enrichment observed in protruding oxide particles.

EDX point analysis at a protruding particle (Spectrum 2) yielded 46.89 at. % O, 17.56 at. % Nb, 14.79 at. % Cr, 4.39 at. % Fe, 5.72 at. % Al, and 10.36 at. % C. The Nb:O atomic ratio of ≈ 0.375 (17.56/46.89) is close to the stoichiometric value for Nb_2O_5 (0.40), suggesting the presence of a high-valence Nb oxide. However, the ratio is also within range for NbO_2 (0.50), particularly given the concurrent detection of Cr that may form Cr_2O_3. The local Nb concentration represents an enrichment of ~65× compared to the bulk Nb content (0.27 at. %), with Nb accounting for ≈ 41% of the total detected metal atoms at the spot. These findings strongly indicate Nb segregation and Nb-oxide formation at the protrusions. As EDX provides only semi-quantitative accuracy for oxygen and the protrusions also contain mixed Cr/Fe/Ni species, definitive phase identification will require follow-up high-resolution analyses such as transmission electron microscopy (TEM) coupled with EDX analyzer.

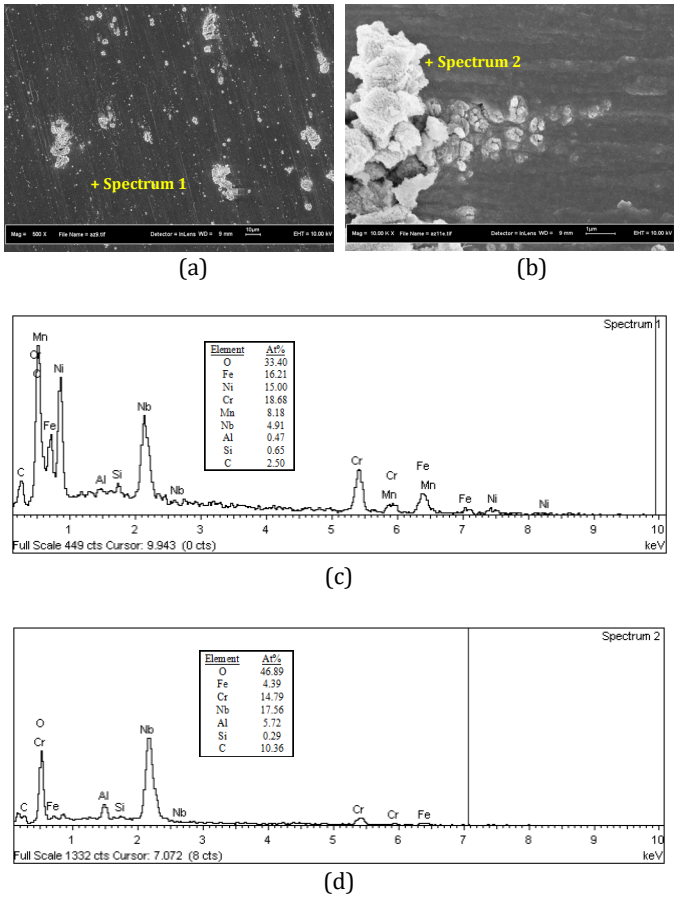

Figure 8. Surface morphology of the low grain diameter (LGD) sample at (a) 500x magnification and (b) 10,000x magnification after 500 hours of isothermal oxidation at 500 °C observed by field emission scanning electron microscopy (FESEM). The corresponding EDX spectra for the LGD sample at (c) spot Spectrum 1 and (d) spot Spectrum 2, identify the elemental composition at the indicated analysis spots.

Other studies have documented surface enrichment of Cr and Nb in alloy materials in oxidation research on Ni-based superalloys, particularly highlighting the development of Nb_2O_5 oxide structures. This phenomenon generally results in a layered oxide scale with a Cr-rich outer layer and a Nb-rich sublayer, in which Cr_2O_3 and Nb_2O_5 are the primary phases, and Nb enrichment is often detected within the Cr_2O_3 layer [17].

The exact Nb-oxide phase could not be conclusively identified by XRD due to the localized nature of these protrusions, which likely fall below the detection threshold. However, based on previous research [4], Nb-rich oxides in

similar Fe-Ni-Cr alloys are commonly recognized as NbO_2. The elevated carbon content detected in some regions is likely associated with MC-type carbide precipitates existing in the alloy. The construction of MC-type carbide precipitates, particularly TiC, NbC and (Nb,Ti)C in the Fe-Ni-Cr alloy system has been documented in our past studies [21]. These carbides act as Nb reservoirs, supplying Nb ions that facilitate the formation of Nb-rich oxides at the protrusion regions, as founds in this study.

Overall, the protruding white oxide particles were confirmed to be Nb-rich phases based on the aforementioned analysis. A diffusion model was developed to further discuss the formation mechanism of protrusion oxides.

FESEM images with EDX spectra analysis of the GD sample are shown in Figure 9. The low magnification images at 500x (Figure 9a) display a homogeneous oxide layer with circular protrusions of white oxide particles, which were further analysed by EDX at Spectrum 3. The higher magnification images at 10,000x (Figure 9b) focus on the oxide spallation area. Elemental composition analysis of the spalled region (Spectrum 1, Figure 9c) revealed the presence of O, Fe, Cr, Nb, Al, Si, and C. The higher Nb content is associated with Nb-rich oxides. Whereas, the detection of Al contents is associated with the primary Al-oxide layer formed underneath the outer Cr-rich oxide scale. Al ions tend to diffuse inward, forming a subscale Al-rich oxide. This Al-rich oxide scale contributes to the establishment of an internal oxide layer. Comparable findings on the internal oxide layer of Al-rich phases have been documented by other scholars [19-20] and in our past studies [18]. The findings indicated that the addition of Al and Si alloying to the alloy system promoted the formation of Al-rich and Si-rich oxide phases, with oxide growth penetrating into the outer primary scale substrate and acting as an internal oxide. The findings in this study revealed that the spalled oxide regions exposed the internal oxide, as confirmed by EDX, which showed high Al content in these regions, indicating the formation of Al-oxide in the internal oxide layer.

The elemental composition EDX analysis of the outer spallation region (Spectrum 2, Figure 9d) showed higher contents of O, Nb, and C, with lower contents of Fe, Ni, and Cr. This observation indicates that the spalled region was previously composed of Nb-rich oxides with less contributions from Cr-containing oxides. This finding is similar to that found in Spectrum 2 in the LGD sample. This analysis supports the initial assumption that the protruding Nb-rich oxide has a higher growth rate and may form an unstable structure. This mechanically unstable structure may lead to crack propagation on the protruding region, which in some cases leads to a total spalling of the oxide scale. In this study, the exfoliation of Nb-rich oxide protrusion structure will expose the base alloy surface that was previously protected by an oxide scale, and cause an acceleration of the oxidation rate to form fresh new oxide to encapsulate the exposed and exfoliated oxide areas. The higher oxidation rate of the HGD sample is due to repeated exfoliation-reoxidation, as evidenced by the greater weight gain observed at 500 hours (Figure 1).

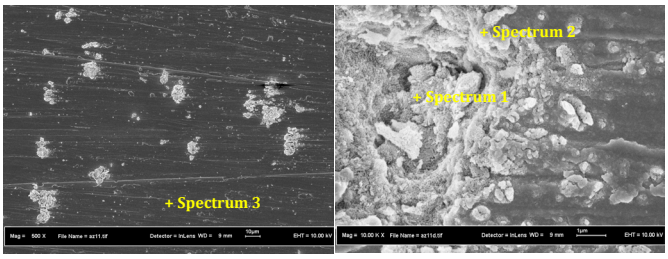

(a) (b)

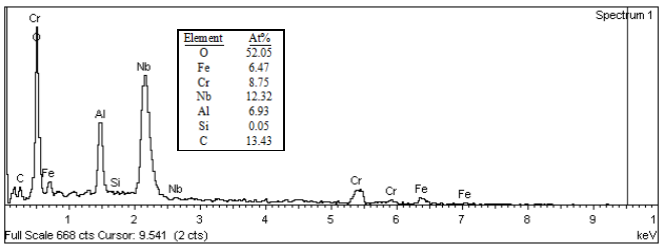

(c)

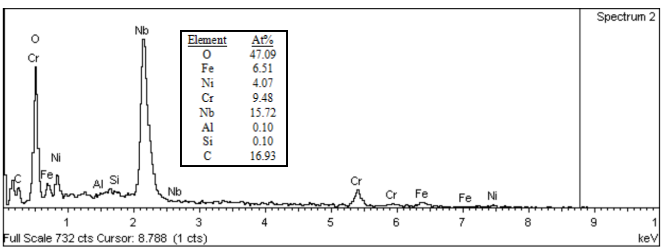

(d)

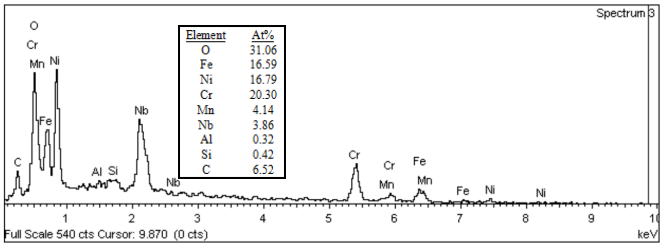

(e)

Figure 9. Surface morphology of the high grain diameter (HGD) sample at (a) 500x magnification and (b) 10,000x magnification after 500 hours of isothermal oxidation at 500 °C observed by field emission scanning electron microscopy (FESEM). The corresponding EDX spectra for the HGD sample at (c) spot Spectrum 1, (d) spot Spectrum 2, and (e) spot Spectrum 3, identify the elemental composition at the indicated analysis spots.

EDX analysis of the elemental composition in the matrix region (Spectrum 3, Figure 9e) showed results similar to Spectrum 1 in the matrix of the LGD sample, indicating that the oxide surface had formed several oxide phases. The overall analysis confirmed that the LGD and HGD samples developed similar mixed-oxide phases in the matrix region, primarily consisting of Cr_2O_3, $MnCr_2O_4$, and other Cr-containing spinel oxides.

3.4. Diffusion model

The analysis of oxidation kinetics and oxide growth behavior enabled the development of a diffusion model describing the formation of protruding Nb-oxide structures under LGD and HGD conditions, as illustrated in Figure 10. This schematic model is based on the proposed sequence of oxide formation and does not correspond to specific exposure times. The progression of oxide evolution is divided into four distinct stages: stage 1 is the nucleation of oxide particles during the initial oxidation stage; stage 2 is the planar oxide growth along the surface as the nuclei coalesce; stage 3 is the perpendicular oxide growth associated with oxide thickening and protrusion development, and lastly stage 4 is the later-stage instability of protruding Nb-oxides.

SA stage 1 ff oxide particle nucleation, during initial oxidation, fine oxide nuclei form across the alloy surface. When a metal alloy is exposed to high-temperature conditions, metal ions (M^+) from the base metal diffuse outward toward the metal-air interface and interact with ambient oxygen, forming a Cr-containing oxide nucleus. In addition, the MC-type carbides in the alloy, such as (Nb,Ti)C, will supply Nb ions, which form Nb oxides. Both LGD1 and HGD1 samples display this nucleation behavior, however, the higher grain boundary density in LGD1 samples facilitates a more uniform and finer distribution of oxide nuclei, whereas HGD1 samples show localized nucleation with larger particle spacing. This difference in early oxide distribution lays the foundation for subsequent growth morphologies.

At stage 2, during planar oxide growth, the nuclei coalesce laterally as oxidation progresses, producing a continuous planar oxide layer. The protective scale will dominate at this stage, namely Cr_2O_3 and spinel oxides composed of $MnCr_2O_4$, $NiCr_2O_4$ and $FeCr_2O_4$, and will coexist with the confined Nb-oxide particles. In the LGD2 samples, the higher grain boundary density enhances lateral diffusion and promotes a more uniform planar oxide layer, contributing to a dense, homogeneous scale. On the other hand, the HGD2 samples exhibit lateral oxide growth with some thickness variations, leaving a possible spot of protruding oxide. The phenomenon at this stage is related to the change in weight of LGD and HGD samples at the beginning of the 100-hour oxidation time (Figure 1), where the LGD sample showed a higher weight gain than the HGD sample due to extensive lateral oxide coverage on the surface. As oxidation progresses beyond this stage, lateral growth will continue in the HGD sample until adjacent oxide particles are fully fused, thereby preparing the stage for vertical growth and subsequent protrusion development.

In stage 3, which is the perpendicular oxide growth, the oxide continues to grow as lateral layers form. Vertical oxide growth will enhance the progress of oxide thickening that occurs due to oxygen inwards diffusion and cation outward diffusion from the base metal. Stage 3: Notice the commencement of a protruding structure of Nb-oxide. The LGD3 sample exhibits a prominent protrusion structure of relatively small size and is evenly distributed, with less stress accumulation due to grain-boundary diffusion. On the other hand, HGD3 samples with lower grain boundary density, which promote lattice diffusion, will result in the growth of Nb-oxide protrusion structures. This phenomenon contributes to the mechanical instability of the oxide scale formed in the HGD sample, as shown in the FESEM image in Figure 9.

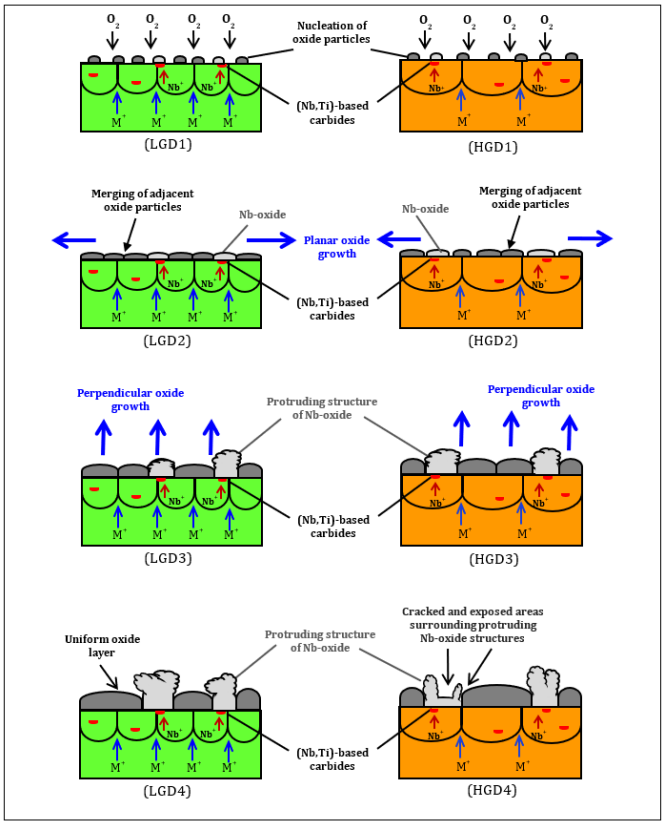

Figure 10. Illustration of the proposed physical diffusion mechanism responsible for the development of protruding Nb-oxide structures in low grain diameter (LGD) and high grain diameter (HGD) samples, showing the influence of grain diameter on the oxide scale growth during high temperature exposure.

Stage 4, the final stage, shows the growth behaviour of the protruding oxide structure in the LGD4 and HGD4 samples. Due to the extensive growth, it causes the structure to protrude outwards in a bigger angular structure which induces localized stresses leading to crack propagation around the protruding structure and may cause subsequent oxide exfoliation. When extensive cracking occurs or worse if the oxide peels off, it will lose the oxide scale revealing localized peeled areas that diminish protection. The peeled scale leaves the alloy surface exposed, triggering rapid re-oxidation and a higher oxidation rate that grows fresh oxide to encapsulate the exposed regions. The higher oxidation rate observed for the HGD sample is attributable to this cyclic exfoliation-reoxidation mechanism, as evidenced by the greater weight gain upon prolonged exposure at 500 hours (Figure 1). In contrast, the LGD4 sample behaved differently, showing a uniform oxide layer and stable protruding oxide structure without excessive growth and restrictive exfoliation, as well as superior protective properties that persisted over prolonged exposure. This stable behaviour of the LGD4 sample can be attributed to a lower oxidation rate, as evidenced by the lower parabolic rate constant shown in Figure 3. As the oxidation growth rate decreases, it facilitates the formation of a stable oxide layer with a homogeneous dispersion of Nb-rich protruding oxide structures that do not cause excessive cracking or exfoliation, as documented by the FESEM images shown in Figure 8.

4. CONCLUSION

In summary, the Nb content in the HR120 Fe-40Ni-24Cr alloy significantly affects the oxidation behaviour of LGD and HGD samples during isothermal oxidation at 500 °C for up to 500 h. A Parabolic oxidation rate law was obeyed by LGD and HGD samples, with a lower parabolic rate constant recorded by the LGD sample of 7.38×10^{-9} $mg^2 \cdot cm^{-4} \cdot s^{-1}$, indicating a lower oxidation rate, hence having good oxidation resistance, which was calculated to be 37% lower than that of HGD sample. Oxides Cr_2O_3 and $MnCr_2O_4$ were recorded by XRD analysis as the dominant phases. Surface morphology analysis using SEM and FESEM documented the distribution of Nb-rich precipitates for the LGD and HGD samples, with the LGD sample exhibiting good scale integrity but evidence of exfoliated oxide in the HGD sample, reducing the protective scale capability. A diffusion model for the growth mechanism of Nb-rich oxide protruding structures has been proposed and consists of four stages. Overall, oxidation resistance improved, with evidence of lower oxidation rate constants and good scale stability, attributable to the lower grain-diameter structure of the LGD sample. Finally, quantitative phase analysis using Rietveld refinement and cyclic oxidation testing are the main focus of our future work to assess long-term durability.

ACKNOWLEDGMENTS

This study was funded by the Ministry of Higher Education Malaysia under Fundamental Research Grant Scheme (FRGS) [FRGS/1/2020/TK0/UNIMAP/02/43].

REFERENCES

[1] J. Cao, Y. Ma, F. Ding, X. Yang, H. Su, Z. Li, W. Qian, J. Cai, B. Jiang, and J. Miao, "Microstructural evolution of Ni-based superalloy GH202 treated by Hf ion implantation during high temperature oxidation," *Journal of Alloys and Compounds*, vol. 1017, 179059, 2025.

[2] C. N. Athreya, K. Deepak, D. I. Kim, B. Boer, S. Mandal, and V. S. Sarma, "Role of grain boundary engineered microstructure on high temperature steam oxidation behaviour of Ni based superalloy alloy 617," *Journal of Alloys and Compounds*, vol. 778, pp. 224-233, 2019.

[3] J. Shi, T. Zhang, B. Sun, B. Wang, X. Zhang, and L. Song, "Isothermal oxidation and TGO growth behavior of NiCoCrAlY-YSZ thermal barrier coatings on a Ni-based superalloy," *Journal of Alloys and Compounds,* vol. 844, 156093, 2020.

[4] N. Parimin, E. Hamzah, and A. Amrin, "Isothermal oxidation behaviour of Ni-based Fe-Ni-Cr superalloys: Role and effect of Nb alloying element," *Springer Proceedings in Physics*, vol. 289, pp. 805-813, 2023.

[5] D. Liu, R. Dong, X. Zhang, Y. Zhang, H. Hou, and Y. Zhao, "High-temperature oxidation behavior of Ni-Cr-W and Ni-Cr-Fe superalloys: A comparative study at 1000 ºC," *Journal of Alloys and Compounds,* vol. 1025, 180271, 2025.

[6] X. Wang, and J. A. Szpunar, "Effects of grain sizes on the oxidation behavior of Ni-based alloy 230 and N," *Journal of Alloys and Compounds,* vol. 752, pp. 40-52, 2018.

[7] M. M. F. N. M. M. Halim, N. Parimin, and E. Hamzah, "Isothermal Oxidation Behaviour of Heat-treated Fe-33Ni-19Cr Series Ni-based Superalloy," *International Journal of Nanoelectronics and Materials,* vol. 17 (special issue), pp. 165–170, 2024.

[8] G. J. Wise, P. M. Mignanelli, M. C. Hardy, N. L. Church, N. G. Jones, and H. J. Stone, "Oxidation Behaviour of New Nickel-Base Superalloys with Varying Aluminium: Niobium Ratio," *High Temperature Corrosion of Materials*, vol. 99, pp. 241–266, 2023.

[9] T. D. Nguyen, J. Zhang, and D. J. Young, "Effect of Mn on oxide formation by Fe-Cr and Fe-Cr-Ni alloys in dry and wet CO_2 gases at 650°C," *Corrosion Science*, vol. 112, pp. 110-127, 2016.

[10] A. Col, V. Parry, and C. Pascal, "Oxidation of a Fe–18Cr–8Ni austenitic stainless steel at 850 °C in O_2: Microstructure evolution during breakaway oxidation," *Corrosion Science,* vol. 114, pp. 17-27, 2017.

[11] W. Wei, S. Geng, G. Chen, and F. Wang, "Growth mechanism of surface scales on Ni–Fe–Cr alloys at 960 °C in air," *Corrosion Science*, vol. 173, 108737, 2020.

[12] Y. X. Xu, J. T. Lu, X. W. Yang, J. B. Yan, and W. Y. Li, "Effect and role of alloyed Nb on the air," *Corrosion Science*, vol. 127, pp. 10-20, 2017.

[13] Y. X. Xu, J. T. Lu, W. Y. Li, and X. W. Yang, "Oxidation behavior of Nb-rich Ni-Cr-Fe alloys: Role and effect of carbides precipitates," *Corrosion Science,* vol. 140, pp. 252-259, 2018.

[14] C. Zhao, Y. Zhou, X. Xing, S. Liu, X. Ren, and Q. Yang, "Precipitation stability and micro-property of (Nb,Ti)C carbides in MMC coating," *Journal of Alloys and Compounds*, vol. 763, pp. 670–678, 2018.

[15] L. Zhang, Q. Yang, J. Chen, M. Zhang, and C. Xiao, "Synergy of γ′ phase, MC carbide and grain boundary phase on creep behavior for nickel-based superalloy K439B," *Materials Science and Engineering: A*, vol. 915, pp. 147261, 2024.

[16] G. D. Smith, and S. J. Patel, "The Role of Niobium in Wrought Precipitation-Hardened Nickel-Base Alloys," *The Minerals, Metals & Materials Society,* 2005.

[17] S. H. Ha, J. Choi, and D. H. Kim, "Investigating Oxide Formation and Growth in Inconel 718 Oxidized at High Temperatures," *Journal of Nanoelectronics and Optoelectronics*, vol. 19, pp. 1007-1010, 2024.

[18] N. Parimin, and E. Hamzah, "Internal Oxidation Behavior of Fe-33Ni-19Cr Alloy," *Materials Science Forum*, vol. 1010, pp. 40-45, 2020.

[19] J. Zurek, D. J. Young, E. Essuman, M. Hansel, H. J. Penkalla, L. Niewolak, and W. J. Quadakkers, "Growth and adherence of chromia based surface scales on Ni-Base alloys in high- and low-pO2 gases," Materials Science and Engineering A, vol, 477, no. 1-2, pp. 259-270, 2008.

[20] A. Chyrkin, W. J. Nowak, K. O. Gunduz, I. Fedorova, M. Sattari, J. Froitzheim, M. Halvarsson, and K. M. Stiller, "Intergranular oxidation of additively manufactured Ni-base alloy 625: The role of Si," *Corrosion Science*, vol. 219, 111234, 2023.

[21] N. Parimin**,** and E. Hamzah, "Influence of Solution Treatment Temperature on the Microstructure of Ni-based HR-120 Superalloy," *IOP Conference Series: Materials Science and Engineering*, vol. 957, 012003, 2020.